A new algorithm of muon scattering tomography based on Multi-Wire Drift Chambers system*

J.L. Zhang,[1,2] X.M. Liu,[2,3,4] Z.Y. Sun,[2,3,5,6] F. Fang,[2,3] Q. An,[2,3] F.H. Lu,[2] S.W. Tang,[2,3] H.R. Yang,[2,3] P. Ma,[2,3] Y. Qian,[2,3] J. Kong,[2,3] S.T. Wang,[2,3] X. Jiang,[2,3] Y.Z. Sun,[2,3] D. Yan,[2,3] X.H. Zhang,[2,3] Y.J. Zhang,[2,3,†] Y.H. Yu,[2,3,5,6,‡] and J. Jiang[1,§]

[1]*College of Physics and Electronics Engineering,Northwest Normal University, Lanzhou 730070, China*
[2]*Institute of Modern Physics, Chinese Academy of Sciences, Lanzhou 730000, China*
[3]*School of Nuclear Science and Technology, University of Chinese Academy of Sciences, Beijing 100049, China*
[4]*School of Nuclear Science and Technology,Lanzhou University, Lanzhou 730000, China*
[5]*Advanced Energy Science and Technology Guangdong Laboratory, Huizhou 516000, China*
[6]*Heavy Ion Science and Technology Key Laboratory, Institute of Modern Physics, Chinese Academy of Sciences, Lanzhou 730000, China*

Cosmic ray muons, characterized by their high energy and penetrative capabilities, provide significant advantages for non-destructive imaging applications, including security inspection, geological exploration, and archaeology. As the muon tomography continues to advance, there is growing demand for precise and efficient muon imaging algorithms. The quality of muon scattering imaging depends on the accuracy of the muon trajectory reconstruction. This paper proposes a neural network-based method utilizing Multi-Wire Drift Chambers (MWDCs), achieving a spatial resolution of 351 μm. Additionally, to address challenges of imaging accuracy and track utilization efficiency, an improved method based on the PoCA (Point-of-Closest Approach) algorithm is introduced. This enhancement significantly improves imaging resolution and reconstruction performance, offering a more solution for muon-based imaging solutions.

Keywords: muon tomography, track reconstruction, neural network, multi-wire drift chambers

I. INTRODUCTION

As the high-energy cosmic rays interact with earth's atmosphere and the generated cascade shower descend towards the earth's surface, in which the production of pi mesons and subsequent decay into muons occur. Cosmic ray muons are unstable elementary particles of two charge types: positive (μ^+) and negative (μ^-). They have a spin of $1/2$, a mass approximately 207 times that of the electron, and a lifetime of 2.2 μs [1]. The flux of muons at sea level is approximately 60-70 $m^{-2}s^{-1}sr^{-1}$, with an average energy range of 3–4 GeV [2, 3].Cosmic ray muons, which are readily accessible natural sources, possess high energy and small interaction cross-sections. Due to these unique physical properties, they can penetrate high-Z materials [4–7] and reach depths of several hundred meters underground, making muon imaging widely applicable in fields such as security inspection for nuclear materials, geological exploration, and archaeology [8]. Muon imaging algorithms can be broadly categorized into two types: absorption-based algorithms [9, 10] and those based on the principle of Multiple Coulomb Scattering (MCS) [2, 11]. Absorption-based algorithms are widely used in geology and archaeology [12–15], with one famous application being the discovery of a hidden chamber in Khufu's pyramid in Egypt [16]. MCS-based algorithms, such as the Point of Closest Approach (PoCA) algorithm proposed by Los Alamos National Laboratory (LANL) [2], are widely applied. Muon scattering-based imaging systems have been developed, such as the Gas Electron Multiplier (GEM) detectors used by Kondo et al. [17, 18], the Multi-gap Resistive Plate Chamber (MRPC) developed by Tsinghua University [19, 20], and the Triangle Scintillator Bars (TSB) by Lanzhou University [21]. The accuracy of the incident and outgoing muon trajectories is crucial for muon imaging systems based on MCS principles.

The Institute of Modern Physics, Chinese Academy of Sciences (IMPCAS), has developed a muon imaging platform based on Multi-Wire Drift Chambers (MWDCs), which provides excellent position resolution, detail description in Section II. A key advancement of this platform is the implementation of a self-supervised neural network method for muon track reconstruction. Unlike traditional methods that rely on simulated data for labeling, this method utilizes the intrinsic characteristics of experimental data to train the neural network, achieving precise muon trajectory imaging without the need for external simulation-based annotations. This data-driven approach significantly improves the practicality and efficiency of muon imaging systems, particularly when simulated data may be unavailable or insufficient. The method for reconstructing muon trajectories based on the neural network is detailed in Section III.

Numerous research institutions worldwide have achieved significant results in developing algorithms, such as MLSD [22], MAP [23], GRA [24], Path Algorithm [25] and so on. In spite of this, the PoCA algorithm is still widely used due to its simplicity and computational efficiency. However, PoCA has notable limitations, including reduced accuracy in vertical direction because some closest points are reconstructed outside the object, which leads to large number of noise point generated and more test time cost to accumulate effective events.

* Supported by the National Natural Science Foundation of China (Grant.), CAS Key Technology Talent Program, and the Guangdong Basic and Applied Basic Research Foundation (Grant No. 2023B1515120067).; Supported by the State Key Laboratory of Heavy Ion Science and Technology, Institute of Modern Physics, Chinese Academy of Sciences, Lanzhou 730000, China

† Corresponding author, zhangyj@impcas.ac.cn
‡ Corresponding author, yuyuhong@impcas.ac.cn
§ Corresponding author, jiangjun@nwnu.edu.cn

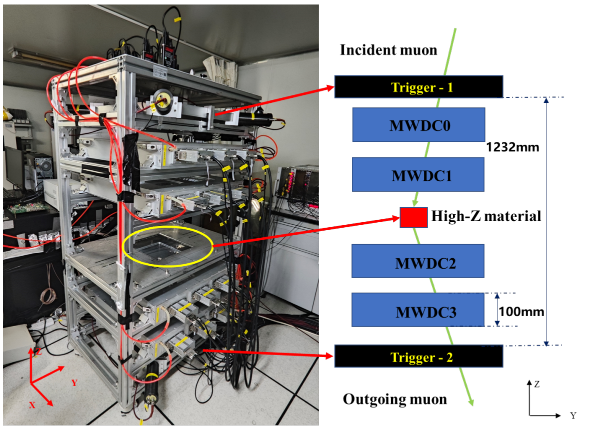

Fig. 1. Multi-Wire Drift Chamber Muon Imaging Platform and 2D Plane Schematic Diagram(YZ_palne)

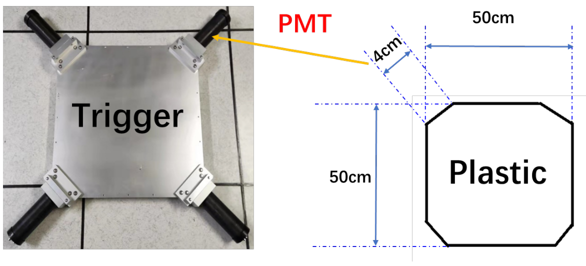

Fig. 2. Large-area plastic scintillator trigger detector. (Left): Physical photograph; (Right): Diagram of shape parameters.

To address these challenges, fewer statistical events are used to locate the general outline of the object, and then the closest point outside the object is corrected back into the object. By refining the traditional PoCA strategy, we effectively enhanced the utilization efficiency of muon tracks and improved the accuracy of scattering angle distributions, bringing them closer to theoretical expectations. The improved PoCA algorithm is discussed in Section IV.

II. THE MUON IMAGING SYSTEM BASED ON MWDCS

We have constructed a muon imaging system based on MWDCs, which offers the information of muon trajectories and are the premise of muon imaging. The detector part of system consists of four identical MWDCs and two large area plastic scintillator detectors. As depicted in the right plot of Fig. 1, the scintillator detectors are positioned at the top and bottom of the system. The detectors have dimensions of 500 mm $\times$ 500 mm $\times$ 30 mm. As shown in Fig. 2, triangular cuts with a base length of 4 cm are made at each corner of the detectors. The scintillation signals are read by PMTs coupled to the corners, providing trigger signals and determining the start or stop time $t_{trigger}$. The four MWDCs with the effective detection area of 40 cm $\times$ 40 cm are divided into two groups, MWDC0 and MWDC1 are responsible for constructing muon incident trajectories above the detection area, while

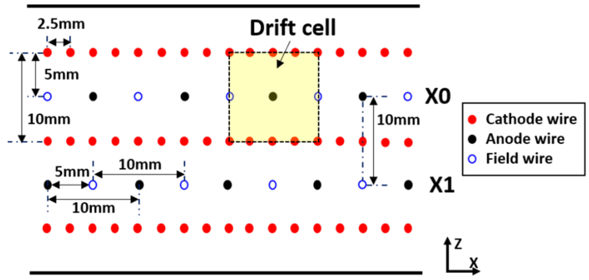

Fig. 3. Schematic diagram of the arrangement of field wires and cathode wires surrounding the anode wire in the same direction, along with the drift cell configuration

MWDC2 and MWDC3 are responsible for the outgoing trajectories below the detection area. Taking the bottom surface of MWDC3 as the position where Z = 0, the positions of the multi-wire drift chamber and the plastic scintillator detectors are shown in Fig. 1

The MWDC is composed of four layers of anode wires generating the readout signal. These layers include two layers aligned in the X direction (X0/X1) and the other two layers aligned in the Y direction (Y0/Y1), which are perpendicular to each other. Each layer contains a total of 40 anode wires, made of 20 μm diameter gold-plated tungsten. Fig. 3 illustrates the structure diagram of the MWDC, showing the arrangement of drift units along the X direction. Within the same layer of anode wires, the spacing between adjacent anode wires is 10 mm, and a field wire is positioned between them. The vertical spacing between the upper and lower anode wires is 5 mm, with a layer of cathode wires placed at each position. Both the cathode and field wires are constructed from 100 μm diameter beryllium copper alloy. The anode wires with the operate voltage of +1200 V, is surrounded by field wires and cathode wires with operate voltage at -300 V, which forms a drift cell, meanwhile the MWDC operates with a gas mixture of 80% argon (Ar) and 20% carbon dioxide (CO_2). When cosmic ray muon passes through the MWDC, secondary electrons produced through the ionization of the mixed gas drift towards the anode wire under the influence of electric field, thereby inducing a readout signal. A MWDC contains 160 drift cells. For the imaging system, totally 640 channels readout signals from 640 drift cells will be preprocessed by front end electronics (FEE) and then transmitted to the time measuring circuit based on HPTDC chip [26, 27] installed on the PXI [27, 28] system. The time t_{wire} recorded from the anode wires is used to calculate the drift time t_{drift} via the formula $t_{drift} = t_{wire} - t_{trigger} - t_{distance}$. Since cosmic ray muons travel at speeds close to the speed of light, $t_{distance}$ can be computed using the distance between the scintillator detector and the anode wires of the drift cell. The time delay from the signal generation on the anode wires to the electronic transmission is neglected here.

III. TRACK RECONSTRUCTION ALGORITHM BASED ON NEURAL NETWORK

A. Data Preprocessing

Assuming the trajectory of cosmic ray muons is a straight line, their 3D tracks can be described by combining linear functions on XOZ and YOZ planes, as illustrated in formula.

$$\begin{cases} x = k_{xoz}z + b_{xoz} \\ y = k_{yoz}z + b_{yoz} \end{cases} \tag{1}$$

Where z represents the vertical position of the fired anode wires (also regarded as hits), while x and y stands for horizontal positions on XOZ and YOZ planes respectively. In ideal conditions, each anode wire layer would produce at most one hit, allowing for straightforward path reconstruction. However, the detection process is not without its challenges. The MWDC's detection efficiency is not perfect, and spurious hits can arise from various sources, such as noise, the diffusion of ionized electrons from adjacent drift cells, or interference from other particles. These factors can result in multiple hits on a single anode wire layer, increasing the total number of hits across all layers. The track system consists of 4 MWDCs with 8 layers of anode wires in x direction. When a cosmic ray muon passes through the MWDCs, it is assumed that the number of layers registering at least one hit is n^x ($n^x \leq 4$), and the number of hits in the i-th layer is n_i. To address this complexity, the exhaustive method is employed to identify all possible hit combinations from these n^x layers on the XOZ plane. The total number of such combinations is given by the product:

$$n_{xoz} = \prod_{i=0}^{n^x-1} (n_i + 1) \tag{2}$$

All the candidate hits combination are obtained using the method mentioned above. Subsequently, selection criteria are applied to filter out combinations caused by noise or other factors. Given that muon imaging relies on incident and outgoing tracks, it is crucial to ensure accuracy of these tracks by confirming at least one hit per anode wire layer. Once the hits for each layer have been identified, the least squares method (LSM) is utilized to perform a linear fit on the remaining hit combinations. This fitting aims to obtain the shortest distance d_i between each hit point and the fitted linear function within i-th layer. The shortest distance d_i within each layer should not beyond the size of the drift cell, namely 5 mm. The ultimate goal of this step is to confine the fitted line to the drift cell where the hit occurred, thereby selecting high quality of hits combination. Similarly, the same principles can be applied to the YOZ plane.

B. Self-supervised Neural Network Training

In the initial phase of track reconstruction, the candidate tracks are derived by fitting the combination of hits using the LSM. However, this preliminary track serves merely as a foundational approximation. To achieve a track with enhanced resolution and improved accuracy, the integration of drift time information, measured by the multi-wire drift chamber, is indispensable. This additional temporal data allows for further optimization and refinement of the preliminary track, thereby significantly elevating the precision and reliability of the final reconstructed track. Once the drift time is known, the drift distance can be determined using the R-T relationship, which is expressed as $r^{drit} = R(t)$. In an ideal scenario, the hit point serves as the center of a circle, with the drift distance r representing the radius. The circumference of this circle corresponds to the position of ionization within the drift cell of a muon, such that the track is tangent to the circle. However, in practical applications, the minimum distance r^{fit} from the hit point to the fitted track often deviates from the drift distance r^{drift}. As shown in Fig. 4, to quantify this discrepancy, we define the fitting residual Δr_i for the i-th hit point as:

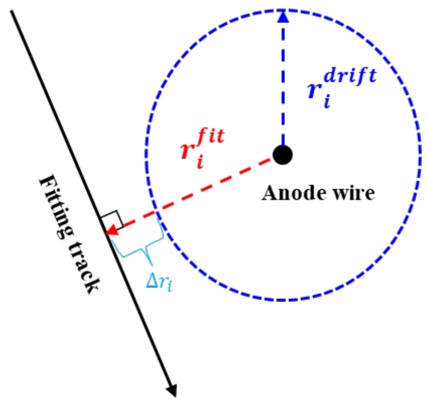

Fig. 4. Fitting Residual Diagram

$$\Delta r_i = r^{\text{fit}} - r^{\text{drift}} \tag{3}$$

And the total residual(MSE) can be expressed as:

$$\chi = \sum_{i=0}^{n^x-1} \Delta r_i^2 / n^x \tag{4}$$

which is vital to the self-supervised neural network.

A self-supervised neural network has been developed to autonomously train on experimental data by without relying on simulation data as labels. The architecture of network, illustrated in Fig. 5, comprises three convolutional layers, one pooling layer, and two fully connected layers[29]. Following the completion of the data preprocessing, initial R-T relationship, hit position $(x, z)/(y, z)$, and their associated drift time t_{drift} were utilized as input to the network. The data passes through the three convolutional layers, where it is transformed into higher feature representations. A max-pooling layer subsequently extracts global features, which are then condensed to represent the parameters of a straight

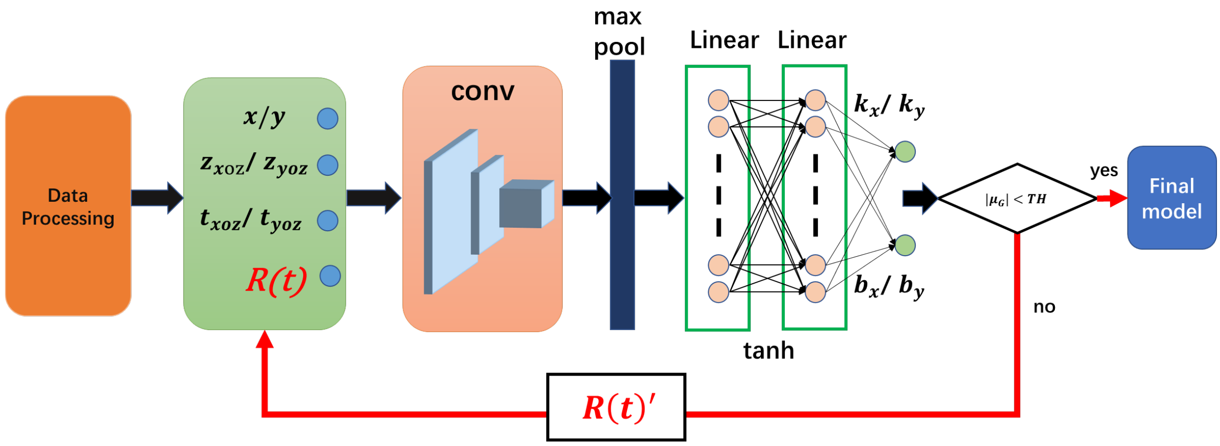

Fig. 5. Neural Network Model Structure Diagram

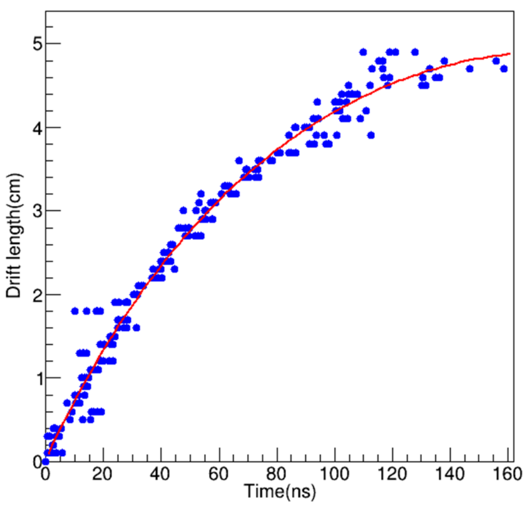

Fig. 6. The R-T relationship simulated by Garfield++

line, characterized by the slope k and intercept b. Training the network requires an initial R-T relationship, which can be derived from Garfield++ simulation software [30, 31]. Garfield++ integrates with the numerical library Magboltz to model complex processes such as gas discharge, drift motion, and signal response. These functionalities are frequently applied to study drift cells by adjusting cell parameters according to the actual parameters of MWDCs. The primary contribution to the signal in the drift cell comes from the ions generated and to the drift time comes from the electrons during the ionization process. Using Garfield++, the initial R-T relationship for the muon within a drift cell is fitted using polynomial function. Fig. 6 shows the relationship between the drift distance and time for a single drift cell under the influence of the electric field.

In the following section, we present the detailed implementation process for training the neural network to get the final model.

Step A: When a muon traverses the muon imaging system, it generates a muon event. After data preprocessing, three key parameters are extracted: the hit position (x_i, z_i) and (y_i, z_i), and the drift time t_i. The experimentally measured dataset is then partitioned into a training set and a test set at an 8:2 ratio.

Step B: The network is subsequently trained using the training set. Meanwhile the $R(t)_1$ relationship, simulated by Garfield++, is used as the initial label for the training data, as illustrated in the network architecture diagram (Fig. 5).

Step C: The predicted distance from the fit line to the hit point is r^{fit}, and the drift distance, derived from the $R(t)_1$ relationship used during training, is r^{drift}. The residual χ is defined as equation 4 mentioned above , and a new $R(t)_2$ relationship is fitted based on r^{fit} and t_i.

Step D: Replace the $R(t)_1$ relationship with the newly obtained $R(t)_2$ relationship, and then repeat Step B and Step C until the residual Δr_i, following a Gaussian distribution with a mean value less than the threshold TH (a typical value is 20 μm).

C. Analysis of Neural Network Prediction Results

To validate the prediction results of the neural network, a test was conducted on the muon imaging system without object installed in detection area. The trained model was applied to the test set, and the residuals were calculated as described by Equation 3. These residuals follows a Gaussian distribution, enabling the determination of the system's spatial resolution. As shown in Fig. 7, the spatial resolution, calculated by using dual-Gaussian fitting approach [32, 33], improved from the initial 621 um to 351 um. Additionally, the system's trigger detectors are two large-area plastic scintillators located above and below the detection area. Each scintillator is a square-shaped with dimensions of 500mm $\times$ 500mm $\times$ 30mm and features four cut-away corners. The unique geometry of the scintillator can be reconstructed by the predicted muon tracks. The results, presented in Fig. 8, clearly

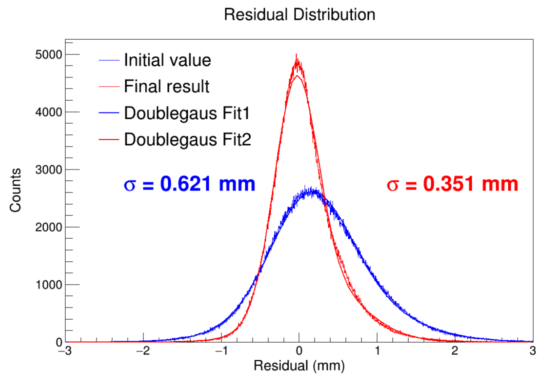

Fig. 7. Double Gaussian fitting for system resolution.

show the reconstructed shape of the scintillator, including the dimensions of the four cut-away corners. This reconstruction further validates the accuracy of the model's predicted tracks. In the absence of an object, the upper and lower MWDCs record the track for the same muon event, which theoretically should form a single straight line. However, due to systematic errors, the two lines may exhibit slight deviations in slope. For each muon event, a pair of tracks from the upper and lower segments is projected onto two orthogonal planes (XOZ and YOZ), and the angular difference between these tracks is calculated. The distribution of these angular differences is compiled into a histogram and fitted with a Gaussian function to determine the system's angular resolution, which is estimated to be approximately 6.2 mrad. The Gaussian fit for angular resolution is shown in Fig. 9.

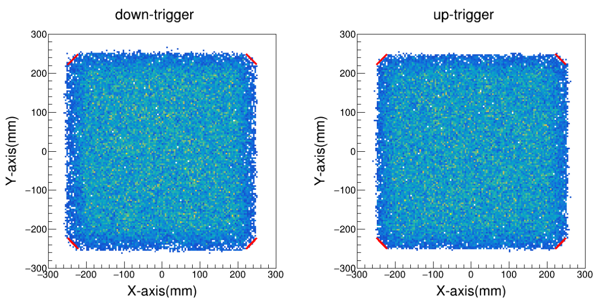

Fig. 8. Schematic diagram of the positions of the upper(left) and lower(right) layer tracks on the trigger

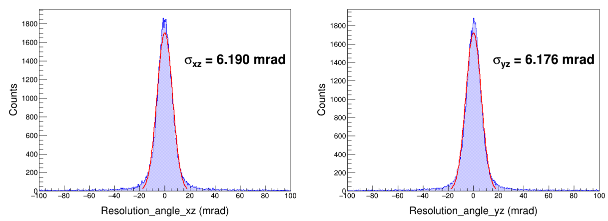

Fig. 9. The angular resolution of the detection system(The left image shows the angular resolution in the xz plane, while the right image shows the angular resolution in the yz plane)

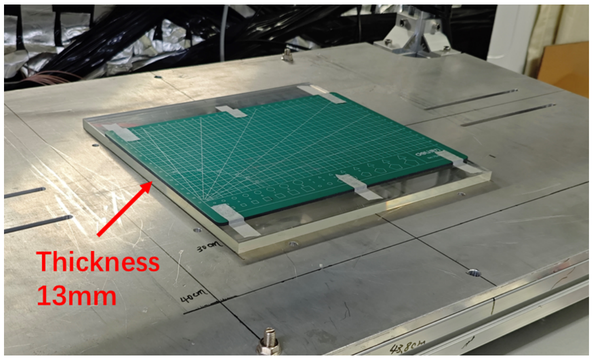

Fig. 10. Placement position of supporting materials

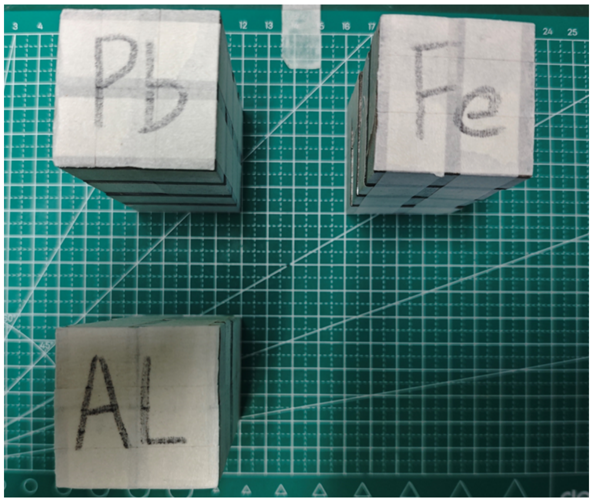

Fig. 11. The objects are symmetrically placed around the center of the detection region.The center coordinates of the Pb block, Fe block, and Al block in the xy-plane are, respectively:(-40mm,-40mm),(-40mm,40mm),(40mm,-40mm)

IV. A RAPID MUON IMAGING METHOD BASED ON IMPROVED POCA ALGORITHM

A. Experimental Materials

Based on a muon imaging test platform with excellent angular resolution, three metal materials were selected to evaluate the performance of the improved Point of Closest Approach (PoCA) algorithm. The objective was to leverage high-quality muons' track events to achieve rapid imaging and material identification for these materials. The three materials, each with a unit size of $2cm \times 2cm \times 2cm$, included aluminum ($Z = 13$), iron ($Z = 26$), and lead ($Z = 82$), representing low-Z, medium-Z, and high-Z materials, respectively. The purity of iron and lead exceeded 99%, while that of aluminum was greater than 97%.

To facilitate the study of the improved PoCA algorithm, a plastic support plate with location markers was positioned at the central position of the test platform for the placement of the three materials. Given the relatively lower Z and density

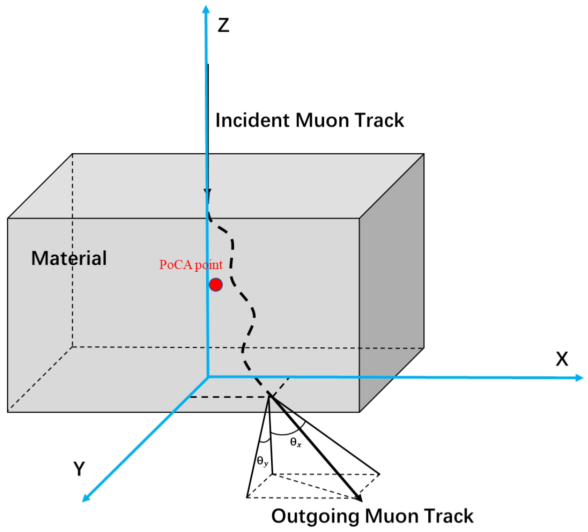

Fig. 12. Schematic Diagram of Muon Multiple Scattering

of the plastic support plate compared to the metal materials, as well as its minimal thickness of 13 mm, the interference caused by the plastic plate on the imaging of the three materials was considered negligible in this experimental setup. Sixteen units of each material were arranged to form a measured object with dimensions of $4cm \times 4cm \times 8cm$, as illustrated in Fig. 10. To ensure that the number of effective muon events passing through each material was approximately equal during the same measured time and to enable a subsequent comparison of the imaging results, the three materials were symmetrically positioned around the center of plastic support plate, as shown in Fig. 11. The precise location of each material was known prior to the measurement.

B. An Improved PoCA Algorithm

As shown in Fig. 12, when a muon traverse a material and undergoes multiple Coulomb scattering, a deviation occurs between its incident and outgoing trajectories. The angles θ_x and θ_y denote the projections of this angular deviation on the X-Z and Y-Z planes, respectively, are statistically independent of each other. The resultant three-dimensional scattering angle θ can be determined by combining θ_x and θ_y. According to Moliere's theory, the scattering angle follows a Gaussian distribution, characterized by a standard deviation δ_{θ_x} [2]. This standard deviation can be calculated using Equation 5, where βc represents the muon's velocity, p its momentum, L the material thickness, and L_{rad} the radiation length of the material. The radiation length, defined as the distance over which a muon loses its energy to $1/e$ of its initial value via bremsstrahlung, can be computed using Equation 6. Equation 7 indicates that the scattering density of the corresponding voxel can be calculated using the voxel-based method. The magnitude of the scattering density can reflect the material of the substance. λ_j represents the scattering density of this voxel, D represents the side length of this voxel, M represents the number of scattering points within this voxel, $p_{r,i}^2$ represents the corrected energy of the muon, and the value of $\Delta\theta_{ij}^2$ is given by Equation 8[2].

These formulation provides a quantitative framework for analyzing muon scattering phenomena in materials, essential for applications in material imaging.

$$\sigma_{\theta_x} = \frac{13.6MeV}{\beta cp}\sqrt{\frac{L}{L_{rad}}}\left[1 + 0.038\ln\frac{L}{L_{rad}}\right] \tag{5}$$

$$L_{rad} = \frac{716.4A}{Z(Z+1)\ln\frac{287}{\sqrt{Z}}}(g.cm^{-2}) \tag{6}$$

$$\lambda_j = \frac{1}{D}\sum_{i=1}^{M}\left(\frac{\Delta\theta_{ij}^2}{M_j} \times \frac{1}{p_{r,i}^2}\right) \tag{7}$$

$$\Delta\theta_{ij}^2 = \frac{\theta_x^2 + \theta_y^2}{2} \tag{8}$$

The Point of Closest Approach (PoCA) algorithm is a widely used method in muon imaging[34, 35], a technique that leverages the scattering behavior of cosmic ray muons to reconstruct the internal structure of objects. The core principle of the PoCA algorithm is to approximate the complex multiple scattering of muons within an object as a single scattering event. This simplification allows the algorithm to determine the scattering point by calculating the closest point between the incident and outgoing muon trajectories, referred to as the PoCA point. By statistically analyzing the distribution of PoCA points from a large number of muon events, the algorithm can infer the object's internal structure and material composition.

The primary advantage of the PoCA algorithm lies in its computational simplicity and efficiency. It enables rapid reconstruction of images from scattering data, making it particularly suitable for real-time imaging applications, especially for high-Z materials (e.g., lead or other dense elements). Despite its advantages, the PoCA algorithm has notable limitations. One significant issue is its reduced accuracy in the Z-direction. During object reconstruction, many PoCA points are erroneously placed outside the object, even though the corresponding muon trajectories pass through it. The algorithm's assumption of treating multiple scatterings as a single event may not accurately reflect the actual muon trajectory, which leads to a low utilization rate of particle tracks, particularly in scenarios with limited cosmic muon counts, reducing the algorithm's overall efficiency.

To address the shortcomings of the PoCA algorithm, an improved PoCA algorithm is proposed. This enhanced method focuses on improving the accuracy of object reconstruction, particularly in the Z-direction, and increasing the utilization efficiency of muons' tracks. The key idea is to leverage the PoCA algorithm to find the high-density regions and preliminarily locate the boundaries of the object. By doing so,

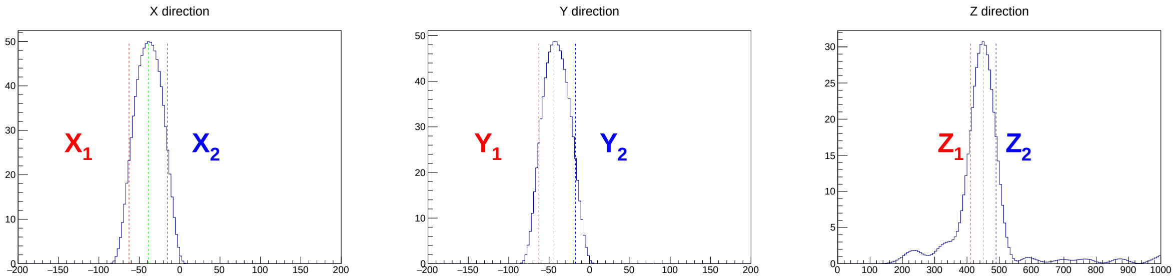

Fig. 13. The determination method for the projections in three directions and the schematic diagram of the two boundaries are shown.

the improved algorithm mitigates the errors associated with the Z-direction and enhances the overall reconstruction quality. The improved PoCA algorithm consists of the following steps:

1.Initial Boundary Identification: The boundaries of the imaged object are determined using the traditional PoCA algorithm, which ensures that scattering points form dense regions within the object. As shown in Fig 13, the boundaries in the XY plane are identified by locating positions with the most significant changes in count rate based on the imaging results, and then the points within the XY boundaries are projected onto the Z-axis, and the positions with the most significant changes in boundary points are calculated to determine the boundaries in the Z-direction. Due to the 6 mrad angular resolution (σ) of the muon imaging system, tracks with small angular deflections ($\theta \leq 3\sigma$) cannot be definitively identified as having been scattered by muons passing through the object. To address this limitation, only tracks with scattering angles greater than 3σ are considered, ensuring high confidence in the selected events.

2.Track Selection: Muon tracks that pass through the object are identified based on the predicted trajectories from the neural network. These tracks are filtered to ensure they intersect the object's boundary.

3.PoCA Point Replacement: The intersection points between the incident and outgoing tracks and the object boundary are calculated. The corrected points, can be spaced at equal intervals along the line connecting the intersection points, are used to replace the PoCA points outside the object for imaging. This step ensures that the reconstructed points lie within the object, addressing the issue of misplaced PoCA points.

C. Applications of the Improved PoCA Algorithm for Rapid Muon Imaging

As mentioned previously, the initial step of the improved PoCA algorithm involves the utilization of large-angle scattering events to delineate the boundary of the object. Given that the physical dimensions and installation position of the object are known priorly, the imaged size and geometric center point derived from the reconstruction are systematically compared with the actual parameters. This comparative analysis serves to quantify imaging errors and assess the accuracy of the reconstruction process, providing a method to evaluate the performance of the improved algorithm.

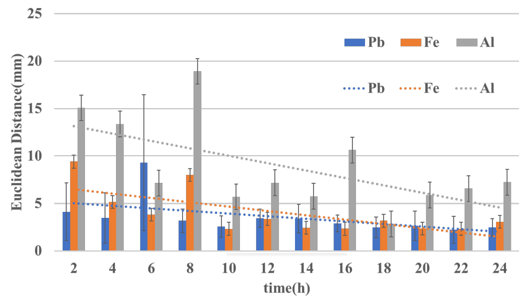

Fig. 14. The position error varies with time

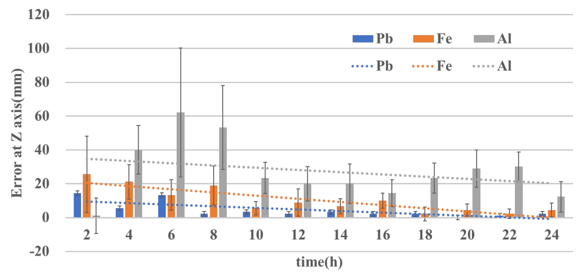

Fig. 15. The Z axis error varies with time

The Euclidean Distance (ED) between the imaged center position and the actual center position is defined by Equation 9, where $\bar{x}$, $\bar{y}$, $\bar{z}$ represent the average values of the imaged central positions from multiple samples with the same imaging duration, and x, y, z stand for the actual central position[36]. Fig. 14 illustrates the variation in the histograms of ED with respect to imaging time. The error bars in the figure are derived from Equations 8 and 11. In Equation 10, x_i represents the central position from i-th sample and $\bar{x}$ means the average central position calculated from multiple samples. Equation 9 defines the standard error (SE) of the samples, which quantifies the precision of the imaged central position.

$$ED = \sqrt{(\bar{x} - x)^2 + (\bar{y} - y)^2 + (\bar{z} - z)^2} \tag{9}$$

$$\sigma = \sqrt{\frac{1}{N-1}\sum_{i=1}^{N}(x_i-\bar{x})^2} \tag{10}$$

$$SE = \frac{\sigma}{\sqrt{N}} \tag{11}$$

Fig. 15 displays the error in the Z-direction, expressed as $|\bar{L_z} - L_z|$, which represents the absolute difference between the imaged and actual sizes of the object in the Z-direction. The error bars in this figure also correspond to the standard error (SE) of multiple samples. Both figures include linear trend lines for the three materials (Al, Fe and Pb), represented by dashed lines. These trend lines are obtained by fitting histogram data with the least squares method.

As shown in Figures 14 and 15, the imaging errors exhibit a decreasing trend as the imaging time increases. For aluminum (Al), due to its low atomic number, the scattering of muons is less pronounced, resulting in fewer scattering points within the region. Consequently, the errors for Al display significant randomness. In contrast, for lead (Pb) and iron (Fe), the imaging results indicate that longer imaging durations improve the precision of boundary localization and overall reconstruction accuracy. The linear trend lines further emphasize the relationship between imaging time and error reduction. This trend is particularly evident for Pb and Fe, where the scattering behavior of muons is more significant compared to Al.

After determining the object boundaries, the PoCA points located outside the object are corrected. Tracks passing through the object region are evaluated, and if the reconstructed point lies outside the selected region, the line segment connecting the intersection points of the incident and outgoing tracks with the boundary is used to replace the original PoCA point. During reimaging process, the voxel method is explored. The line segments are calculated within the same voxel as the remaining PoCA points in the imaging region. A certain number of points are evenly sampled along the line segment, excluding the two endpoints. The computed values within the voxels are normalized, which does not affect the differentiation of object materials. The imaging results are shown in Fig. 16, with the upper image presenting the results from the standard PoCA algorithm and the lower image displaying the results from the improved PoCA method. As shown in Fig. 16, the three-dimensional imaging results of the PoCA algorithm and the improved method are compared for different imaging durations. The improved method effectively relocates scattering points initially imaged outside the object along the Z-direction to within the object boundaries, resulting in a noticeable improvement in the imaging accuracy.

To further validate the improved method, scattering points within the actual measured object's region were selected, and corresponding tracks were analyzed. The scattering angle distributions of the tracks for different materials (Pb, Fe, and Al) were compared between the standard PoCA algorithm and the improved method, as shown in Fig. 17. Based on Molière's theory, Gaussian functions were used to fit the distributions, enabling the determination of the standard deviation of the scattering angles for each material. Theoretically, assuming a muon energy of 3 GeV and considering its velocity as the speed of light, the standard deviation of the Gaussian distribution for the scattering angle was calculated for each material. The theoretical standard deviations are as follows: Pb: 18.2 mrad, Fe: 9.89 mrad, Al: 4.14 mrad. However, due to the system's angular resolution of 6.2 mrad, the theoretical values must account for this resolution. Thus, the adjusted theoretical standard deviations are: Pb: 19.20 mrad, Fe: 11.60 mrad, Al: 7.34 mrad, which align more closely with the experimental results from the improved method. That demonstrates the effectiveness of improved method in enhancing imaging accuracy and material identification.

V. SUMMARY

This paper proposes an improved PoCA algorithm to enhance the accuracy of muon imaging and shorten the imaging time. We developed a self-supervised neural network model based on MWDCs system to predict muon tracks without simulation data as labels. Through the neural network model, a position resolution of 351 um and an angular resolution of 6.2 mrad were successfully achieved. An improvement of the traditional PoCA algorithm is also developed based on predicted muon tracks. The imaging results demonstrate that the improved method significantly enhances the utilization of muon tracks and reduces errors in the Z-direction during object reconstruction, meanwhile identifies materials very well with scattering angle distribution.

[1] Luis Rodolfo Perez Sanchez, Muon Lifetime Measurement in Chiapas and the Escaramujo project. IOP Conf.Journal of Physics. **866**, 012011 (2017) doi:10.1088/1742-6596/866/1/012011

[2] Schultz LJ et al., Image reconstruction and material Z discrimination via cosmic ray muon radiography. Nuclear Inst. and Methods in Physics Research, A **519**, 687-694 (2004). doi: 10.1016/j.nima.2003.11.035

[3] Beringer J, Arguin J F, Barnett R M, et al.,Review of particle physics. l. Phys. Rev.D .**86**, 010001 (2012). doi: 10.1103/PhysRevD.86.010001

[4] Xiao, S et al., A modified multi-group model of angular and momentum distribution of cosmic ray muons for thickness measurement and material discrimination of slabs, Nuclear Science and Techniques, Nucl. Sci. Tech. **29**, 2 (2018). doi: 10.1007/s41365-018-0363-7

[5] Si-Yuan Luo et al., Hybrid model for muon tomography and quantitative analysis of image quality, Nuclear Science and Techniques, Nucl. Sci. Tech. **30**, 120 (2019). doi: 10.1007/s41365-022-01070-6

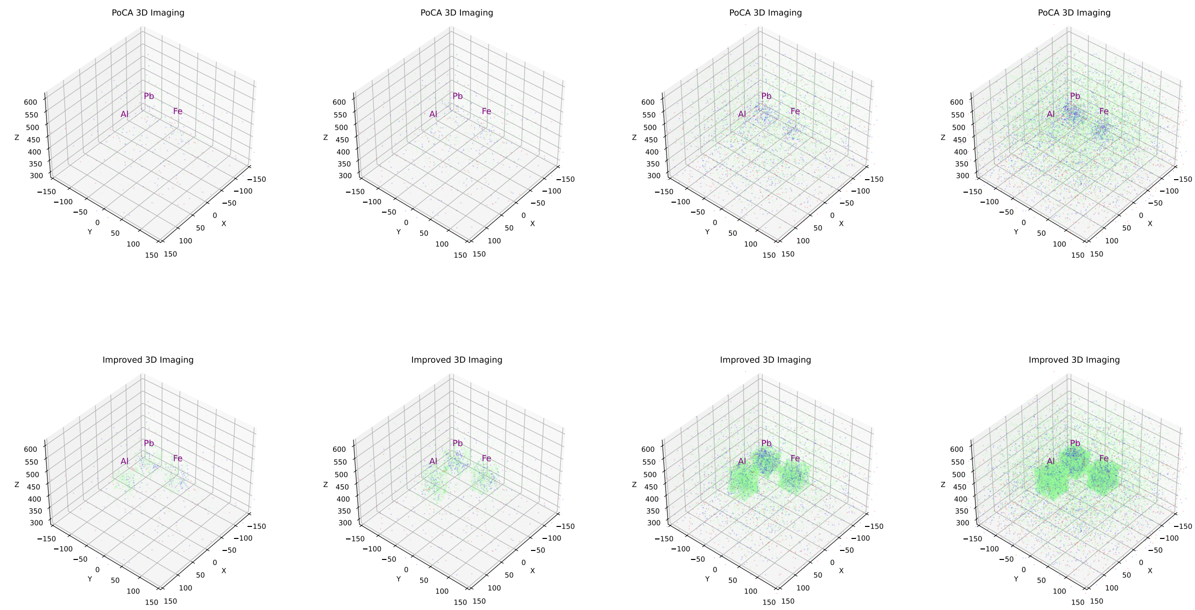

Fig. 16. The figure shows schematic diagrams of three-dimensional imaging after 2, 4, 10 and 24 hours using the PoCA algorithm and the improved method(from left to right). The upper images are the results from the PoCA algorithm, while the lower images show the results from the improved method.

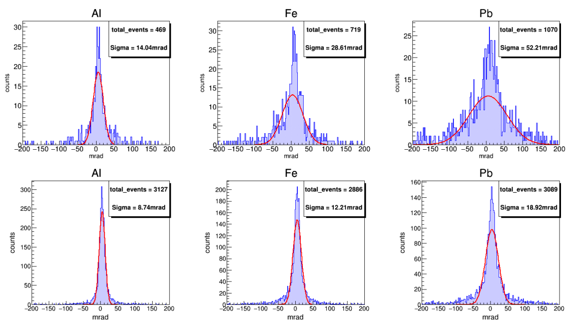

Fig. 17. The figure compares the angle distributions before and after the improvement. The upper plot shows the distribution before the improvement, while the lower plot shows the distribution after the improvement.

[6] S. Riggi,, V. Antonuccio-Delogu et al., Muon tomography imaging algorithms for nuclear threat detection inside large volume containers with the Muon Portal detector. Nuclear Inst. and Methods in Physics Research, A . **728**, 59–68 (2013). doi: 10.1016/j.nima.2013.06.040

[7] LIU Yuanyuan et al., Imaging Algorithms for Cosmic Ray Muon Radiography Detection of Nuclear Materials. Nuclear Inst. and Methods in Physics Research, A . **14**, 3 (2009). doi:10.1016/S1007-0214(09)70046-X

[8] Xing-Yu Pan et al., Experimental validation of material discrimination ability of muon scattering tomography at the TU-MUTY facility, Nuclear Science and Techniques, Nucl. Sci. Tech. **30**, 120 (2019). doi: 10.1007/s41365-019-0649-4

[9] N. Lesparre et al., Geophysical muon imaging: feasibility and limits.Geophys. J. Int. **183**, (2010). doi: 10.1111/j.1365-246X.2010.04790.x

[10] W.B. Gilboy, et al., Industrial radiography with cosmic-ray muons: A progress report,Nuclear Inst. and Methods in Physics Research.**580**, 1 (2007). doi: 10.1016/j.nima.2007.05.191

[11] Xiang, ST et al., A time and charge measurement board for muon tomography of high-Z materials, Nuclear Science and Techniques, Nucl. Sci. Tech. **28**, 3 (2017). doi: 10.1007/s41365-017-0183-1

[12] Cheng, YP et al., Imaging internal density structure of the Laoheishan volcanic cone with cosmic ray muon radiography, Nuclear Science and Techniques, Nucl. Sci. Tech. **33**, 7 (2022). doi: 10.1007/s41365-022-01072-4

[13] Yasushi Yamashina et al., Development of a cost-effective plastic scintillator for cosmic-ray muon radiography of a volcano, Earth Planets Space. **62**, 173-177 (2010). doi: 10.5047/eps.2009.03.003

[14] K.Jourde et al.,Experimental detection of upward going cosmic particlesand consequences for correction of densityradiography of volcanoes, GEOPHYSICAL RESEARCH LETTERS. **40**, 6334-6339 (2013). doi: 10.1002/2013GL058357

[15] Reza DARIJANI et al., A New Approach in Coal Mine Exploration Using Cosmic Ray Muons. Acta Geophysica. **64**, 4 (2016). doi:10.1515/acgeo-2016-0032

[16] Morishima, K., Kuno, M., Nishio, A. et al. Discovery of a big void in Khufu's Pyramid by observation of cosmic-ray muons. Nature 552, 386–390 (2017). doi: 10.1038/nature24647

[17] Gnanvo, K. et al. Detection and imaging of high-Z materials with a muon tomography station using GEM detectors. Proceedings of IEEE NSS/MIC. (2010). doi: 10.1109/NSS-MIC.2010.5873822.

[18] Kondo Gnanvo and Leonard V et al., Imaging of high-Z material for nuclear contraband detection with a minimal prototype of a muon tomography station based on GEM detectors. Nuclear Inst. and Methods in Physics Research **652**, 1 (2010). doi: 10.1016/j.nima.2011.01.163

[19] Fan X, Wang Y, Wang X, et al.,High position resolution MRPC developed for muon tomography. Proceedings of IEEE NSS/MIC. (2012). doi: 10.1109/NSSMIC.2012.6551048

[20] Shi L, Wang Y, Huang X, et al. A high time and spatial resolution MRPC designed for muon tomography. Journal of Instrumentation . **9**, 12 (2014). doi: 10.1088/1748-0221/9/12/C12038

[21] X. Luo, et al., Development and commissioning of a compact Cosmic Ray Muon imaging prototype,Nuclear Inst. and Methods in Physics Research.**1033**, 166720 (2022). doi: 10.1038/nature24647

[22] Schultz LJ et al.,Statistical Reconstruction for Cosmic Ray Muon Tomography. IEEE Trans, Med. Imag.**16**, 8 (2007). doi: 10.1109/TIP.2007.901239

[23] G. Wang, L. J. Schultz and J. Qi,Bayesian Image Reconstruction for Improving Detection Performance of Muon Tomography. IEEE Trans, Med. Imag.**18**, 5 (2009). doi: 10.1109/TIP.2009.2014423

[24] L. Chen, et al., Imaging multi-materials tightly combined objects by applying grey relational analysis in muon tomography, Prog. Nucl. Energy .**154**, 104416 (2022). doi: 10.1016/j.pnucene.2022.104416

[25] Y. Zhao, et al., A cosmic ray muons tomography system with triangular bar plastic scintillator detectors and improved 3d image reconstruction algorithm: a simulation study, Nucl. Eng. Technol.**55**, 2 (2022). doi: 10.1016/j.net.2022.10.031

[26] J. Christiansen, HPTDC High Performance Time to Digital Converter, 2004 http://cds.cern.ch/record/1067476/files/cer-002723234.pdf.

[27] Y.Z. Sun et al., The drift chamber array at the external target facility in HIRFL-CSR. Nuclear Inst. and Methods in Physics Research, A . **894**, 72–80 (2018). doi: 10.1016/j.nima.2018.03.044

[28] PXI-1 hardware specification rev. 2.2. http://www.pxisa.org/userfiles/files/Specifications/PXIHWSPEC22.pdf.

[29] Max Jaderberg and Karen Simonyan and Andrew Zisserman and Koray Kavukcuoglu, Spatial Transformer Networks,arXiv.**1506**, 02025 (2015). doi: 10.48550/arXiv.1506.02025

[30] S.F. Biagi, Nuclear Instruments and Methods in Physics Research Section A: Accelerators, Spectrometers, Detectors and Associated Equipment. Nuclear Inst. and Methods in Physics Research, A . **421**, 234-240 (1999). doi: 10.1016/S0168-9002(98)01233-9.

[31] S.F. Biagi, Magboltz.http://magboltz.web.cern.ch/magboltz/.

[32] J.B. Liu et al., Abeamtest of a prototype of the BESIII drift chamber in magnetic field. and Methods in Physics Research, A . **557**, 436-444 (2006). doi: 10.1016/j.nima.2005.11.093

[33] Zhoubo He et al., Development of the MWDC prototype of the CSR external-target experiment, Nuclear Science and Techniques, Nucl. Sci. Tech. **35**, 174 (2024). doi: 10.1007/s41365-024-01515-0

[34] Ji, Xuan-Tao and Luo, Si-Yuan et al., A novel 4D resolution imaging method for low and medium atomic number objects at the centimeter scale by coincidence detection technique of cosmic-ray muon and its secondary particles, Nuclear Science and Techniques, Nucl. Sci. Tech. **33**, 1 (2022). doi: 10.1007/s41365-022-00989-0

[35] Lie He et al., Simulation and experimental comparison of the performance of four-corner-readout plastic scintillator muon-detector system, Nuclear Science and Techniques, Nucl. Sci. Tech. **35**, 188 (2024). doi: 10.1007/s41365-024-01530-1

[36] Bashar, Md. Khayrul AND Komatsu et al., Automatic Extraction of Nuclei Centroids of Mouse Embryonic Cells from Fluorescence Microscopy Images, Public Library of Science. **7**, 1-18 (2012). doi:10.1371/journal.pone.0035550